

# Non-Boussinesq subgrid-scale model with dynamic tensorial coefficients

Rahul Agrawal,\* Michael P. Whitmore, Kevin P. Griffin, and Parviz Moin<sup>†</sup>  
*Center for Turbulence Research, Stanford University, California, United States of America-94305*

Sanjeeb T. Bose  
*Cascade Technologies, Inc., California, United States of America-94303 and*  
*Institute for Computational and Mathematical Engineering, Stanford University*  
(Dated: April 26, 2022)

A major drawback of Boussinesq-type subgrid-scale stress models used in large-eddy simulations is the inherent assumption of alignment between large-scale strain rates and filtered subgrid-stresses. *A priori* analyses using direct numerical simulation (DNS) data has shown that this assumption is invalid locally as subgrid-scale stresses are poorly correlated with the large-scale strain rates [Bardina *et al.*, AIAA 1980; Meneveau and Liu, *Ann. Rev. Fluid Mech.* 2002]. In the present work, a new, non-Boussinesq subgrid-scale model is presented where the model coefficients are computed dynamically. Some previous non-Boussinesq models have observed issues in providing adequate dissipation of turbulent kinetic energy [e.g.: Bardina *et al.*, AIAA 1980; Clark *et al.* *J. Fluid Mech.*, 1979; Stolz and Adams, *Phys. of Fluids*, 1999]; however, the present model is shown to provide sufficient dissipation using dynamic coefficients. Modeled subgrid-scale Reynolds stresses satisfy the consistency requirements of the governing equations for LES, vanish in laminar flow and at solid boundaries, and have the correct asymptotic behavior in the near-wall region of a turbulent boundary layer.

The new model, referred to as the dynamic tensor-coefficient Smagorinsky model (DTCSM), has been tested in simulations of canonical flows: decaying and forced homogeneous isotropic turbulence (HIT), and wall-modeled turbulent channel flow at high Reynolds numbers; the results show favorable agreement with DNS data. It has been shown that DTCSM offers similar predictive capabilities as the dynamic Smagorinsky model for canonical flows. In order to assess the performance of DTCSM in more complex flows, wall-modeled simulations of high Reynolds number flow over a Gaussian bump (Boeing Speed Bump) exhibiting smooth-body flow separation are performed. Predictions of surface pressure and skin friction, compared against DNS and experimental data, show improved accuracy from DTCSM in comparison to existing static coefficient (Vreman) and dynamic models (dynamic Smagorinsky).

---

\* rahul29@stanford.edu  
† moin@stanford.edu

**Keywords:** Large-eddy simulation; subgrid stress; wall modeled LES; dynamic procedure; Gaussian bump; smooth-body separation

## I. INTRODUCTION

The most commonly used class of subgrid-scale stress models is the eddy-viscosity formulation. Smagorinsky [49] developed a subgrid-scale (SGS) stress closure model using where the subgrid-scale stress are assumed to be aligned and scaled with the local strain rate of the large-scale eddies. This model produces satisfactory results in simulations of decaying homogeneous isotropic turbulence [31, 37]; however, the modeled SGS stress does not vanish in laminar regions nor near solid walls, making it unsuitable for simulating transitional or wall-bounded flows. To account for near-wall scalings, the model was modified by prescribing damping functions [39, 45] that return the correct asymptotic behavior near solid boundaries. Germano et al. [17] developed the dynamic Smagorinsky model (DSM) in which the model coefficient is dynamically computed from the local flow state without any prescribed coefficients, improving the predictive capability of LES. The dynamic variant of the Smagorinsky model was shown to accurately dissipate energy from the large-scales in simulations of isotropic decaying turbulent flow, and appropriately vanish in laminar and transitional flows [44]. However, to ensure numerical stability, a regularization procedure, such as clipping or spatial averaging, is often required to be applied to the dynamically computed model coefficient [18].

To avoid challenges that arise in complex flows and on unstructured grids, such as the construction of test filters or the definition of homogeneous averaging operations, more sophisticated static-coefficient models have been proposed. These models attempt to embed properties such as appropriate asymptotic near-wall scaling [41], vanishing eddy viscosities in laminar regions [42, 53], or minimum sufficient dissipation of small-scale turbulence [47]. While these models have reduced computational complexity compared to their dynamic counterparts, they have been seen to have relatively weaker predictive capability. For instance, recent simulations of flows around realistic aircraft models have shown that the dynamic Smagorinsky model offers more accurate predictions of integrated quantities of interest (e.g., lift, drag) and salient flow features (e.g., separation bubble extents) [19].

Lastly, most investigations into the construction of subgrid-scale models for large-eddy simulation have focused on their performance in homogeneous isotropic turbulence and wall resolved LES limits. The resolution of viscously scaled eddies near the wall is prohibitively expensive at high Reynolds numbers and recent advances have shown the relatively successful application of wall modeled LES approaches to practical engineering flows [7]. In many of these wall modeled LES calculations, detailed comparisons of different subgrid-scale models have not been available [20].

This investigation proposes a novel, dynamic subgrid-scale model that accounts for the misalignment of subgrid stresses and resolved strain rates through the introduction of a tensorial eddy viscosity in contrast to traditional isotropic eddy viscosity closures. It is shown that this tensorial eddy viscosity better correlates with the local subgrid stress (in *a priori* tests) and offers similar accuracy to existing dynamic models in isotropic limits (homogeneous turbulence). Detailed *a posteriori* testing of this model is focused on high Reynolds number limits where interactions of SGS and wall models have to be considered. For this, we discuss the performance of the proposed model in both canonical (turbulent channel flow) and complex flow exhibiting separation. In these wall modeled LES calculations, the dynamic tensorial SGS models outperform existing static and dynamic coefficient models.

This paper is organized as follows. We revisit the existing SGS formulations in Section 2, and then present the proposed modeling approach in Section 3. The details of the various numerical solvers used in this study are provided in Section 4. *A priori* results from these models including the stress tensor and kinetic energy dissipation based correlations between modeled and exact stresses for turbulent channel flow are presented in Section 5. Asymptotic behavior of the proposed model near a solid wall and in laminar channel flow are discussed in Section 6. Detailed *a posteriori* analysis of the performance of these models in isotropic turbulence and high Reynolds number channel flows is presented in Section 7. The model is subsequently applied to a flow over a Gaussian bump exhibiting separation and comparisons of the surface pressure and skin friction between WMLES and spanwise-periodic quasi-DNS and 3D experiments are presented in Section 8. Concluding remarks are offered in Section 9.

## II. LES FORMALISM AND GOVERNING EQUATIONS

In LES, the large-scale quantities are defined by filtering the velocity and pressure fields. If the grid-filter kernel operator is denoted by  $\mathcal{G}$ , then a large scale quantity,  $\bar{f}$  is evaluated from the total field,  $f$  as,

$$\bar{f}(x) = \int \mathcal{G}(x, x') f(x') dx' \quad (1)$$

where the integral is extended to the entire computational domain. Further, we assume that the grid filter is such that it commutes with the differentiation operation. More details on LES formalism can be found in previous studies [17, 18, 53].

The governing equations for LES of incompressible turbulent flows (of constant density  $\rho$ ) are obtained by applying the aforementioned filter to the Navier-Stokes equations. The resulting equations are

$$\frac{\partial \bar{u}_i}{\partial x_i} = 0 \quad (2)$$

and

$$\frac{\partial \bar{u}_i}{\partial t} + \frac{\partial \bar{u}_j}{\partial x_j} \bar{u}_i = -\frac{1}{\rho} \frac{\partial \bar{p}}{\partial x_i} + \nu \frac{\partial^2 \bar{u}_i}{\partial x_j \partial x_j} - \frac{\partial \tau_{ij}^{sgs}}{\partial x_j}, \quad (3)$$

where  $\tau_{ij}^{sgs} = \bar{u}_i \bar{u}_j - \bar{u}_j \bar{u}_i$  is the subgrid stress which requires modeling closure. The isotropic component of the SGS stress is often absorbed into pressure, which leads to a pseudo-pressure field ( $p \mapsto p + \rho \tau_{kk}^{sgs}$ ). The eddy viscosity based SGS closure models based on the Boussinesq hypothesis take the form

$$\tau_{ij}^{sgs} - \frac{1}{3} \tau_{kk} \delta_{ij} = -2\nu_t \bar{S}_{ij}, \quad \text{where } \bar{S}_{ij} = \frac{1}{2} \left( \frac{\partial \bar{u}_i}{\partial x_j} + \frac{\partial \bar{u}_j}{\partial x_i} \right). \quad (4)$$

where  $\delta_{ij}$  is the Kronecker-delta function. Two of the more commonly used Boussinesq models that are examined in this study are the Smagorinsky model with its dynamic variant and the Vreman model, which are described in detail below.

### A. Smagorinsky model

The units of eddy viscosity are a velocity times a characteristic length scale. Smagorinsky's [49] celebrated eddy viscosity model is based on a length scale proportional to the LES grid scale and a velocity scale obtained from the product of the grid scale and the magnitude of the strain-rate tensor. With these assumptions, the eddy viscosity is given as

$$\nu_t = (C_s \Delta)^2 |S|, \quad \text{where } |S| = \sqrt{2\bar{S}_{ij} \bar{S}_{ij}} \quad (5)$$

and  $\Delta$  is the grid filter width. Later, Lilly [30] showed that for isotropic turbulence with spatial resolution that lies in the inertial subrange,  $C_s \sim 0.17$ . Deardorff [14] recommended  $C_s \sim 0.1$  in turbulent shear flows. The applicability of this model is limited, especially in the near-wall region of wall-bounded flows in part because eddy viscosity does not vanish at the wall. Consequently, previous studies [39] have used wall-damping functions [51] to correct for the behavior of eddy viscosity in the viscous sublayer.

### B. Dynamic Smagorinsky model

Germano et al. [17] introduced the notion of test filtering of the LES governing equations. Through the use of these ideas, the Leonard stress tensor [29],  $L_{ij} = -\widehat{\bar{u}_i \bar{u}_j} + \widehat{\bar{u}_i} \widehat{\bar{u}_j}$  ( $\widehat{(\cdot)}$  denotes test-filter operation) can be related to the resolved stress as

$$L_{ij} = 2(C_s \Delta)^2 \left( \frac{\widehat{\Delta}^2}{\Delta^2} \widehat{|S|} \widehat{S}_{ij} - \widehat{|S|} \widehat{S}_{ij} \right) = 2(C_s \Delta)^2 M_{ij}, \quad (6)$$

where  $\widehat{\Delta}$  and  $\Delta$  denote test-level and grid-level filter widths, respectively. For an incompressible flow, Eq. (6) is an over-determined system with five independent equations for one undetermined coefficient. Lilly [32] proposed a least-squares solution of this system, leading to the expression for the model coefficient

$$(C_s \Delta)^2 = \frac{L_{ij} M_{ij}}{2 M_{ij} M_{ij}}. \quad (7)$$

To avoid numerical instabilities arising from the computation of negative eddy viscosities ( $C_s < 0$ ), the numerator and denominator of this equation are averaged in statistically homogeneous directions (and possibly time for statistically stationary flows) to give its working form

$$(C_s \Delta)^2 = \frac{\langle L_{ij} M_{ij} \rangle}{\langle 2M_{ij} M_{ij} \rangle}, \quad (8)$$

where  $\langle \cdot \rangle$  is the spatio-temporal averaging operator.

### C. Vreman model

Vreman [53] proposed a modified subgrid-scale model by including the velocity gradient tensor and the gradient model expansion of the exact SGS tensor, leading to the model form

$$\nu_t = 2.5(C_s)^2 \sqrt{\frac{B_\beta}{\alpha_{ij} \alpha_{ij}}} ; \quad \alpha_{ij} = \frac{\partial \bar{u}_i}{\partial x_j} ; \quad \beta_{ij} = \Delta^2 \alpha_{mi} \alpha_{mj} ; \quad (9)$$

$$B_\beta = \beta_{11} \beta_{22} - \beta_{12}^2 + \beta_{11} \beta_{33} - \beta_{13}^2 + \beta_{22} \beta_{33} - \beta_{23}^2 \quad (10)$$

The nominally accepted value of  $C_s \approx 0.17$  is used in the present implementation of this model. Unlike the Smagorinsky model, the Vreman model does not over-predict subgrid dissipation in transitional flows, and also appropriately provides zero subgrid dissipation in laminar flows (in two velocity component base states).

## III. MODELING FRAMEWORK

While the dynamic procedure improves the predictive capability of the constant coefficient Smagorinsky model, it does not resolve the model form error that is inherent to all Boussinesq SGS models (i.e. that the SGS stress is not necessarily aligned with the strain-rate tensor). Additionally, for LES of flows with mean anisotropy, the assumption of a scalar model coefficient, as used in classical Boussinesq eddy viscosity closures, is potentially overly restrictive. In this work, we propose a novel dynamic formulation for the tensor-coefficient Smagorinsky model [38]. This model contains non-Boussinesq terms that do not lead to dissipation but would potentially improve the local alignment between modeled and exact subgrid stresses. Similar to the dynamic Smagorinsky model, the only input parameter in this model is the ratio of test-level to grid-level filter widths, which is chosen to be two as in our previous studies.

### A. Dynamic tensor-coefficient Smagorinsky model (DTCSM)

Moin [38] proposed the following tensor-coefficient-based Smagorinsky model to account for misalignment in DNS between filtered resolved stresses and mean strain rates,

$$\tau_{ij}^{sgs} - \frac{\tau_{kk}^{sgs}}{3} \delta_{ij} = -(C_{ik} S_{kj} + C_{jk} S_{ki}) |S| \Delta^2. \quad (11)$$

This model contains nine independent coefficients, thus providing more degrees of freedom in determining alignment of the stress and strain-rate tensors. However, in its current form, the tracelessness of the model, which is a requirement imposed by the governing equations, is not guaranteed. To treat this, we put the following constraints on the coefficients (see Appendix A for details):

$$C_{11} = C_{22} = C_{33} ; \quad C_{ij} = -C_{ji} \quad (j \neq i) . \quad (12)$$

The realizability constraints reduce the number of independent coefficients from nine to four. Incorporating this reduction, we invoke the Germano identity to arrive at

$$L_{ij} = (C_{ik} \Delta^2 M_{kj} + C_{jk} \Delta^2 M_{ki}). \quad (13)$$

For an incompressible flow, this system of five independent equations with four coefficients is solved using the least-squares solution method [32] to obtain the coefficients dynamically. It is noteworthy that only  $C_{11}$  (and equivalently  $C_{22}, C_{33}$ ) contributes to the dissipation of energy from the large scales.

The reader is directed to Appendices B and C for more details on the dynamic procedure and a brief discussion of how the model form can be expressed explicitly in terms of a combination of strain-rate and rotation-rate tensors.

#### IV. NUMERICAL SOLVER DETAILS

In this paper, two second-order finite-difference solvers with staggered Cartesian meshes are used to simulate homogeneous isotropic turbulence and turbulent channel flow, respectively. These solvers have been validated in previous studies of homogeneous isotropic turbulence [6, 46] and turbulent channel flow [2, 33]. Both employ explicit fourth and third-order Runge-Kutta time integration schemes, respectively.

Simulations of the Gaussian bump are performed using a low-dissipation, explicit, unstructured, finite-volume solver for the compressible Navier-Stokes equations (charLES). This code is formally 2<sup>nd</sup>-order accurate in space and 3<sup>rd</sup>-order accurate in time. Details of the solver and validation cases in subsonic, transonic, and supersonic studies can be found in [8, 16, 22, 28].

#### V. A PRIORI TESTS

In this section, we compare *a priori* performance of DSM and DTCSM at stress tensor and dissipation rate levels with respect to filtered-DNS data (a discretely commutative filter with three vanishing moments [52] is recursively applied to obtain a filter width equal to three times the grid size.) for a channel flow at  $Re_\tau = 395$ . In the presence of flow anisotropy, an improved SGS model is expected to produce higher stress tensor correlations and provide more realistic representation of the small scales. These correlations are defined as

$$\rho = \frac{1}{6} \sum_{k=1}^6 \frac{\text{cov}(\tau_{model,k}, \tau_{exact,k})}{\sigma(\tau_{models,k})\sigma(\tau_{exact,k})}, \quad (14)$$

where  $k = 1, 2, \dots, 6$  are the six components of exact ( $\tau_{exact}$ ) and modeled ( $\tau_{model}$ ) SGS stress tensors. Note that  $\text{cov}(X, Y)$  denotes the covariance between quantities  $X$  and  $Y$  and  $\sigma(X)$  is the standard deviation of the distribution of the quantity  $X$ . The correlations based on the kinetic energy dissipation rate are similarly defined by contracting the stress tensor with the large-scale strain-rate tensor.

Figure 1 shows that DTCSM produces higher correlations than the dynamic Smagorinsky model at the tensor level. It is encouraging that the correlations are most improved near the wall, which is the region of high anisotropy and, in practical calculations, the limiting region in terms of resolution requirements. *A priori* calculations, however, are not completely reflective of the model performance in simulations. The model of Bardina et al. [5] showed much improved tensor-level correlations than even DTCSM; however, it was shown to be significantly under-dissipative in simulations and required ad hoc supplementary dissipation from an eddy viscosity of Smagorinsky form. At the *a priori* level, DTCSM has exactly the same dissipation rate correlation (see Figure 2) as DSM across the entire channel height. This is indeed expected since the only terms in DTCSM that contribute to dissipation are Smagorinsky-type terms. Although not shown, varying the filter width from two times the grid size to up to four times the grid size has indicated little sensitivity in the qualitative trends for both stress tensor and dissipation correlations. A verification of the dissipative aspects of these models in LES is presented next in the *a posteriori* results section.

#### VI. ASYMPTOTIC BEHAVIOR IN LAMINAR FLOWS AND NEAR SOLID WALLS

In laminar flows with sufficient resolution, the Leonard stress approaches zero and consequently, the computed dynamic coefficients will also vanish (which can be confirmed from inspection of Eq. (13)).

Near a solid wall, in the viscous sublayer, universal scalings for all three components of velocities have been well established [27]. Germano et al. [17] reported that the dynamic Smagorinsky model stress in the near-wall region scaled consistent with the distance from the wall. The eddy viscosity at the wall asymptotically reaches zero, and within the viscous sublayer it scales as  $\nu_t \sim y^{+3}$  in this region, leading to the correct order of magnitude estimates for modeled subgrid stress in comparison to DNS.

Assuming a test-filter kernel that does not operate in the wall-normal direction, and using velocity scalings from DNS as  $u^+ \sim y^+$ ,  $v^+ \sim y^{+2}$  and  $w^+ \sim y^+$ , the scalings for  $L_{ij}$ ,  $M_{ij}$  can be written in terms of distance from the wall in inner units. On solving the resulting system of equations in Appendix B, it can be shown that for DTCSM,  $C_{11} \sim y^{+3}$ ,  $C_{12} \sim y^{+2}$ ,  $C_{13} \sim 0$ ,  $C_{23} \sim y^{+2}$ . With these results, it can be easily inferred that the subgrid shear stress asymptotically reaches zero at the wall following the expected scaling  $\tau_{12}^{sgs} \sim y^{+3}$ . Thus, the behavior of the proposed models in near-wall region is in agreement with asymptotic near-wall scalings.

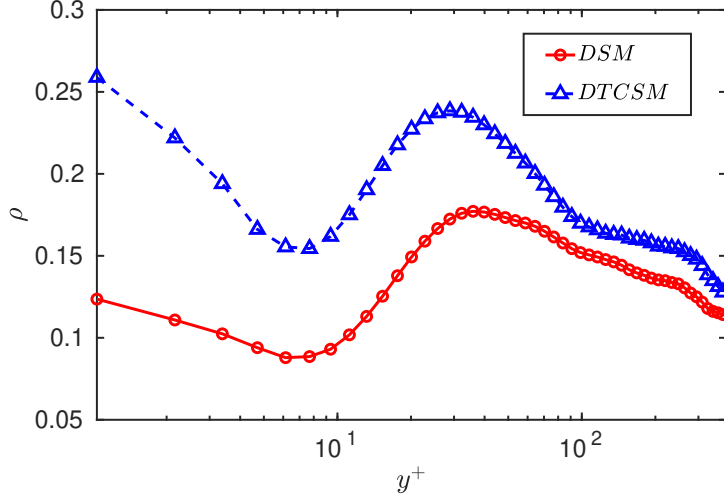


FIG. 1. Stress tensor correlations of DSM and DTCSM with respect to filtered DNS of turbulent channel flow at  $Re_\tau = 395$ .

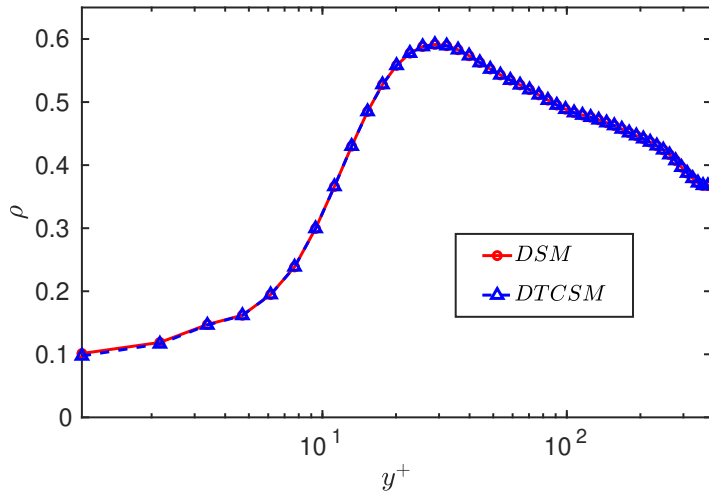


FIG. 2. Dissipation rate correlations of DSM and DTCSM with respect to filtered DNS of turbulent channel flow at  $Re_\tau = 395$ .

## VII. A POSTERIORI CALCULATIONS

Large eddy simulations with DTCSM are performed for decaying and forced homogeneous isotropic turbulence (HIT), and turbulent channel flow and the results are compared with DNS and LES with the DSM closure.

### A. Decaying homogeneous isotropic turbulence

We perform DNS and LES of decaying HIT [13] at  $Re_\lambda = u_{rms}\lambda/\nu = 70$ . The initial turbulent field follows the spectrum in Passot and Pouquet [43], with  $u_{rms} = 1$ . For a triply-periodic box of size  $(2\pi)^3$ , the DNS is performed on a grid of  $128^3$  resolution while LES is performed using a coarser grid containing  $32^3$  points. For HIT, the turbulent kinetic energy ( $tke$ ) and dissipation rate ( $\epsilon$ ) are defined as

$$tke = \left\langle \frac{1}{2}u_i u_i \right\rangle \text{ and } \epsilon = \left\langle 2\nu \bar{S}_{ij} \bar{S}_{ij} - \tau_{ij}^{sgs} \bar{S}_{ij} \right\rangle \quad (15)$$

where  $\langle \cdot \rangle$  is the volumetric-averaging operator. In Figures 3 and 4, we compare the evolution of kinetic energy and

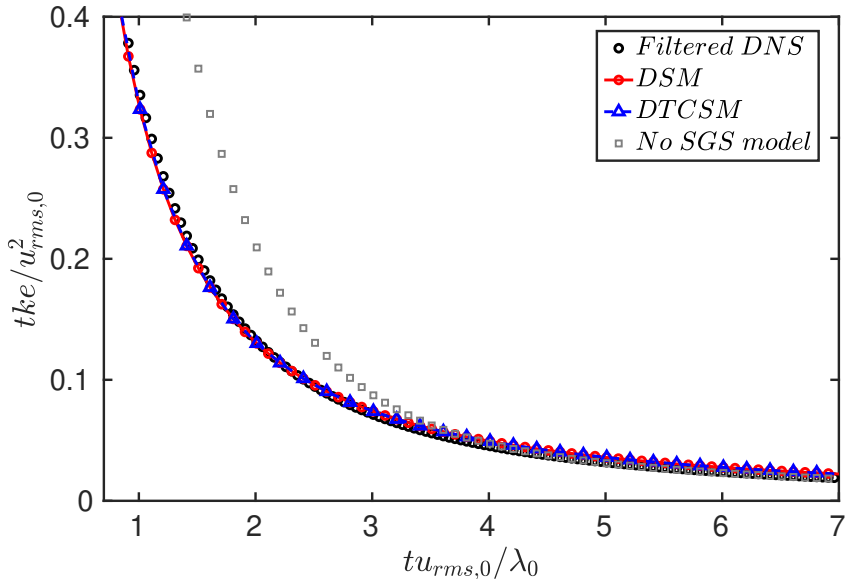


FIG. 3. Evolution of turbulent kinetic energy for decaying isotropic turbulence.

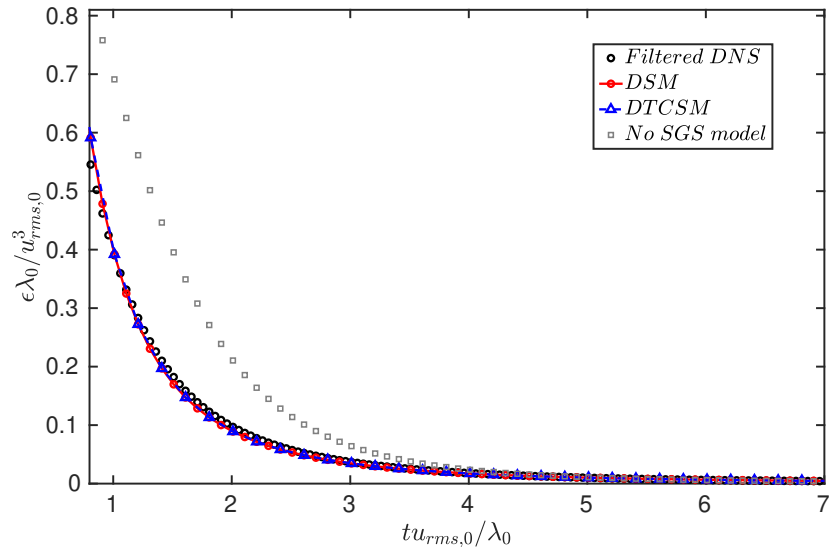


FIG. 4. Evolution of the turbulent kinetic energy dissipation rate for decaying isotropic turbulence.

the dissipation rate in LES to the filtered DNS. Since the calculation without an SGS model does not dissipate enough kinetic energy, it is apparent that the SGS models are needed to properly dissipate turbulent kinetic energy. The time evolution of both  $tke$  and  $\epsilon$  with both of the LES models are in excellent agreement with the filtered DNS after the initial transient (of up to one eddy turn-over time, due to a random-phase based initialization of the velocity field in spectral space). The exponent of the decay of turbulent kinetic energy,  $\alpha$ , when  $tke \sim t^\alpha$  for DSM and DTCSM is  $\alpha \sim -1.33$  and  $-1.35$  respectively and is in reasonable agreement to the decay rate of the filtered DNS,  $\alpha \sim -1.37$  (filtered using a box filter of filter width equal to the LES grid size). It is then apparent that DTCSM dissipates energy as well as DSM without any *ad hoc* modifications to the dynamic procedure. It should be noted that some existing constant-coefficient non-Boussinesq SGS models [5, 12] under-dissipate energy in such calculations and require augmentation from a Smagorsky-model-type term.

### B. Forced homogeneous isotropic turbulence

We now compare LES of forced HIT at  $Re_\lambda = 315$  with  $128^3$  grid points with the filtered DNS of Cardesa et al. [10] performed with  $1024^3$  grid points. A linear momentum forcing is applied to maintain constant turbulent kinetic energy in the system [6].

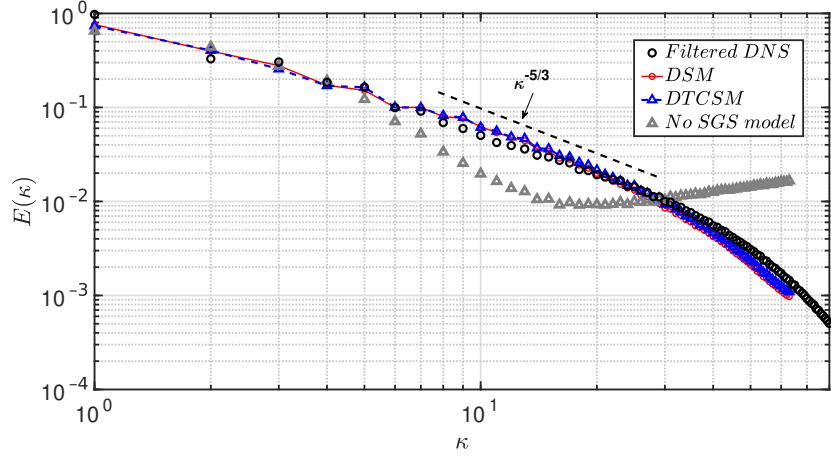


FIG. 5. Comparison of kinetic energy spectra,  $E(\kappa)$ , in forced isotropic turbulence between filtered-DNS and SGS models. The resolution of the filtered-DNS is at  $1024^3$  compared to the LES resolution of  $128^3$ .

Three-dimensional energy spectra are compared in Figure 5, where the  $\kappa^{-5/3}$  scaling is well recovered by both DSM and DTCSM. The energy spectra for LES also compare very well with the filtered DNS (evaluated using a box filter of filter width equal to LES grid size). This agreement suggests that the proposed models transfer energy from the largest scales to the inertial subrange as expected and hence on average do not show any scale-to-scale spurious energy transfer. Since the flow does not have large-scale global anisotropy, it is also expected that the performance of DSM would be similar to that of DTCSM, which is consistent with our results.

### C. Homogeneous isotropic turbulence in the limit $Re_\lambda \rightarrow \infty$

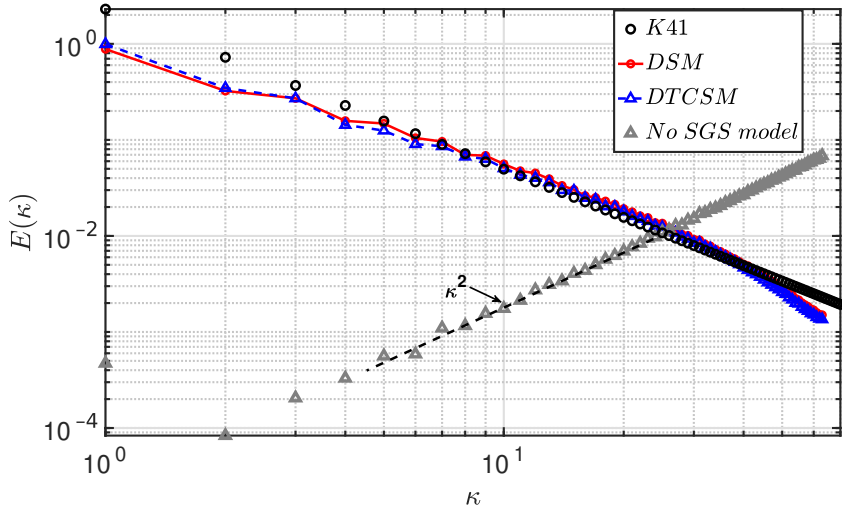


FIG. 6. Comparison of kinetic energy spectra,  $E(\kappa)$ , between filtered-DNS and SGS models as  $Re_\lambda \rightarrow \infty$ . The LES resolution considered here is  $128^3$ .

Simulation	$N_x$	$N_y$	$N_z$	$\Delta x^+$	$\Delta y_{min}^+$	$\Delta y_{center}^+$	$\Delta z^+$
DNS	3072	1081	3072	12.8	0.31	10.7	6.4
WMLES	128	40	64	200	200	200	200

TABLE I. Simulation parameters for turbulent channel flow at  $Re_\tau = 4200$

In the limit of  $Re_\lambda \rightarrow \infty$ , multiple decades of the  $K41$  scaling (i.e.,  $E \sim \kappa^{-5/3}$ ) are expected across the spectrum. From Figure 6, it is evident that the  $K41$  scaling is well recovered with DTCSM (as well as DSM), further confirming both their dissipative nature and inter-scale energy transfer properties. The  $\kappa^2$  scaling in the absence of an SGS model is observed consistent with the principle of equipartition of energy.

#### D. Wall-modeled LES of channel flow

In this section, we investigate the performance of DTCSM in a channel flow at  $Re_\tau = u_\tau \delta / \nu = 4200$ , where  $u_\tau$  is the friction velocity and  $\delta$  is channel half-height. Lozano-Durán and Jiménez [35] performed DNS of this flow with grids as refined as  $\Delta x^+ = 12.8$ ,  $\Delta y_{min}^+ = 0.31$  and  $\Delta z^+ = 6.4$  in inner units. For practical WMLES calculations, the grid resolutions are specified in outer units, and grid resolutions of 20 – 60 points ( $\Delta y^+ \sim 60 – 200$ ) across the boundary layer have been previously used [33]. In this work, we use 20 points per half-height of the channel.

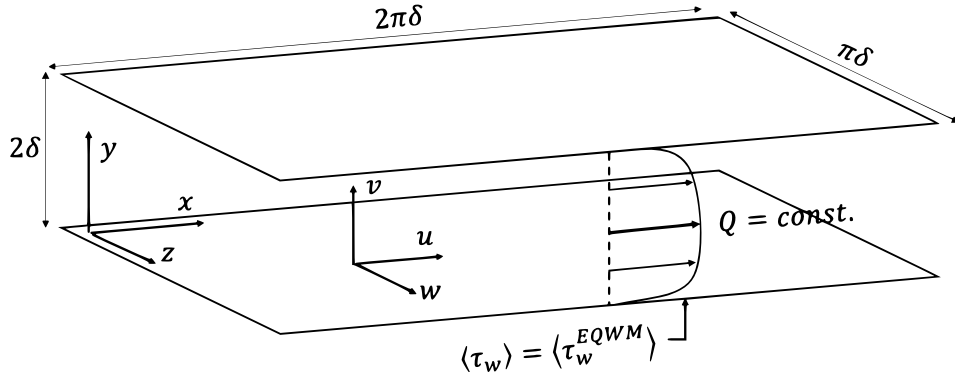


FIG. 7. Schematic of the channel-flow WMLES setup.

Figure 7 shows the schematic of the channel flow and domain sizes in the three directions. Table I summarizes the simulation parameters used in the DNS reference and the present WMLES. The channel is driven at constant mass-flow rate to match the mass flow from DNS. Since in viscous dominated region near the wall is under resolved, the equilibrium wall model by Cabot and Moin [9] with second point matching [26] ( $y^+ \sim 300$ ) is used in conjunction with the SGS model.

From Figure 8, DTCSM is slightly better than DSM at predicting the mean streamwise velocity profile throughout the logarithmic region. Specifically, in the log layer, the error in the prediction of the Kármán constant ( $\kappa = 0.38$  predicted by DNS) is lowered from 10% off with DSM to a 5% error with DTCSM. The over-prediction of the mean streamwise component of intensity in the near-wall region with respect to unfiltered DNS in LES of channel flows has been a concern; WMLES is expected to under-predict the intensity in order to be consistent with filtered DNS. In Figure 9, it is observed that the streamwise and wall-normal components of turbulent intensities with DTCSM are lower than those with the DSM near the wall, which is a qualitative indicator that the prediction is improving when compared to turbulence fluctuations based on unfiltered DNS (explicitly filtered DNS data is not used here similar to previous work of Lozano-Durán and Bae [2, 33]). It must be noted that improvements in the over-prediction of streamwise intensities have also been previously reported using a slip (Robin) boundary condition for a lower Reynolds number [3].

For a turbulent channel flow driven at  $Re_\tau$  as low as 395, Morinishi and Vasilyev [40] observed that DSM requires ad hoc clipping in the near-wall region. A similar trend is observed at  $Re_\tau = 4200$  in our simulations (Figure 10), where the subgrid stresses in the second off-wall point are clipped. No such clipping was necessary with the DTCSM.

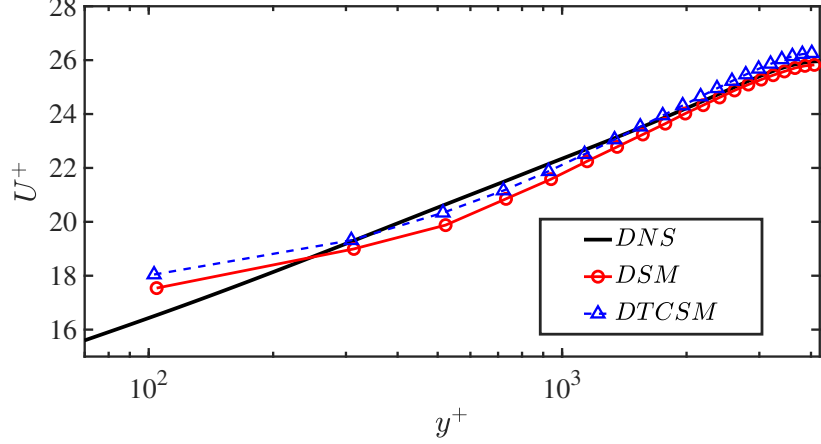


FIG. 8. Wall-normal profiles of mean streamwise velocity for DSM and DTCSM in turbulent channel flow at  $Re_\tau = 4200$ .

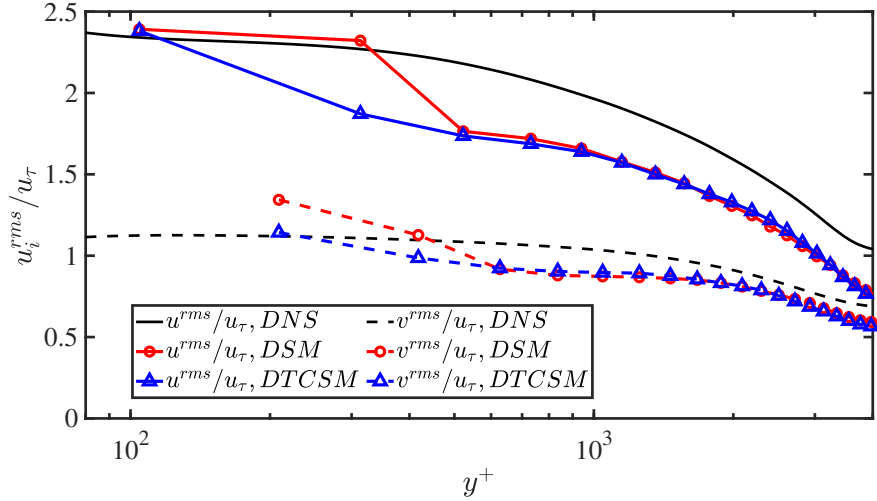


FIG. 9. Wall-normal profiles of turbulent intensities for DSM and DTCSM in turbulent channel flow,  $Re_\tau = 4200$ . The curves without symbols represent the mean intensities from DNS.

### VIII. WALL-MODELED LES OF FLOW OVER GAUSSIAN BUMP

Next, the subgrid-scale models are deployed in the simulation of flow over a wall-mounted Gaussian bump (also known as the Boeing speed-bump [55]). The geometry of the bump was proposed by Boeing and Williams et al. [55]. The bump surface is defined by an analytical expression,  $h(x, z)$ , written as

$$h(x, z) = \frac{h_0}{2} e^{-(x/x_0)^2} \left\{ 1 + \operatorname{erf} \left[ \left( \frac{L}{2} - 2z_0 - |z| \right) / z_0 \right] \right\}, \quad (16)$$

where  $x$  and  $z$  are the streamwise and spanwise coordinates, respectively. The bump width,  $L$ , is used to scale the other dimensions of the bump, as well as define a Reynolds number,  $Re_L$ . Here,  $h_0 = 0.085L$  is the maximum height of the bump, and  $x_0 = 0.195L$  controls the Gaussian decay of the surface in the streamwise direction. Figure 11 is a schematic of the bump as a function of streamwise and spanwise coordinates.

In this flow, the turbulent boundary layer is subjected to both favorable and adverse pressure-gradadients leading to the formation of a separation bubble. Experimental results [23] have revealed approximate Reynolds number independence for pressure and skin-friction coefficients. Due to the presence of side walls and the associated mean three-dimensionality in the flow, and the availability of experimental data, the Boeing speed bump is a good candidate for assessing the predictive capability of LES models in a smooth-body separation.

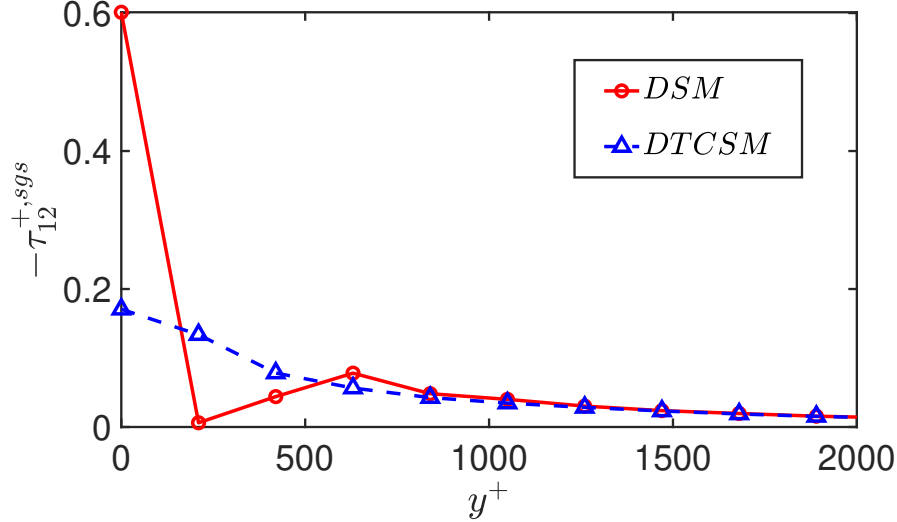


FIG. 10. Wall-normal profiles of mean SGS shear stress for DSM and DTCSM in WMLES of turbulent channel flow at  $Re_\tau = 4200$ . Note that a Neumann boundary condition ( $d\tau^{sgs}/dy = 0$ ) at the wall is used to determine the SGS stress there.

Unlike many widely studied canonical separated flows, such as backward-facing steps or bumps which have geometrically-imposed separation points [4, 11, 15, 48], the present geometry features a smooth-body separation whose location and extent is significantly more difficult to predict computationally. In fact, several recent investigations have observed that some existing wall and subgrid-scale models struggle to correctly predict the occurrence/location of separation [24, 54].

In addition to the available experimental data, Uzun and Malik [50] performed a quasi-DNS of the spanwise-periodic variant geometry. For the spanwise-periodic geometry, the height of the bump surface is given by the simplified equation  $h(x) = h_0 \exp(-x^2/x_0^2)$ . In the separated region, the surface pressure is found to agree well with the experiment of Williams et al. [55] along the centerline  $z = 0$ . Further, the skin friction measurements at mid-span for the three dimensional configuration are in good agreement with the spanwise-periodic case [23]. Uzun and Malik [50] refer to their simulation as a quasi-DNS since it obeys the resolution requirements of DNS in the near-wall region and most of the attached boundary layer; however, it is more comparable to LES resolution in the outer part of the boundary layer where the boundary layer becomes thick.

For the spanwise-periodic configuration, the inlet velocity profile, located at  $x/L = -1.0$ , is a mean profile sampled from a RANS computation [50]. The inflow boundary layer is steady before undergoing a numerical transition to turbulence; thus, there is a development length in the WMLES simulation over the region  $-1.0 < x/L < -0.8$ . Free-stream conditions are set at the top boundary for this case. On the other hand, the three dimensional bump configuration has a plug flow inlet at  $x/L = -1.0$  with the side and top boundary conditions treated as inviscid walls to account for the wind tunnel walls. The outlet is located at  $x/L = 2.5$  and  $x/L = 1.5$  in the spanwise-periodic and experimental configurations respectively. A non-reflecting characteristic boundary condition with constant pressure is applied at the outlet. Similar to the turbulent channel flow simulations, an algebraic formulation of the equilibrium wall-stress model is used. The details of the compressible formulation of the equilibrium wall model are skipped here for brevity, and can be found in existing literature [22, 25].

For this flow, the quantities of interest are the skin friction coefficient ( $C_f$ ) and pressure coefficient ( $C_p$ ) which are defined as,

$$C_f = \frac{\tau_w}{1/2\rho_\infty U_\infty^2} \quad \text{and} \quad C_p = \frac{p - p_{\text{ref}}}{1/2\rho_\infty U_\infty^2}. \quad (17)$$

where  $U_\infty$ ,  $\tau_w$ ,  $p$  and  $p_{\text{ref}}$  are the inlet free-stream velocity, mean wall-stress, wall pressure, and reference pressure, respectively. The reference pressure is taken to be the pressure at the wall at  $x/L = -0.83$  to match the reference pressure used by Williams et al. [55].

Both the spanwise-periodic and three-dimensional bumps have the same background mesh spacing,  $\Delta/L = 0.01$ . The grid is a Voronoi diagram generated from the centroids of a hexaongally close-packed lattice. While refining the grid, the control volumes (CVs) are refined homothetically by factors of 2 in layers near the wall boundaries. Each successive mesh has CVs twice as fine as those of the previous mesh. This refinement approach injects a thin layer (10

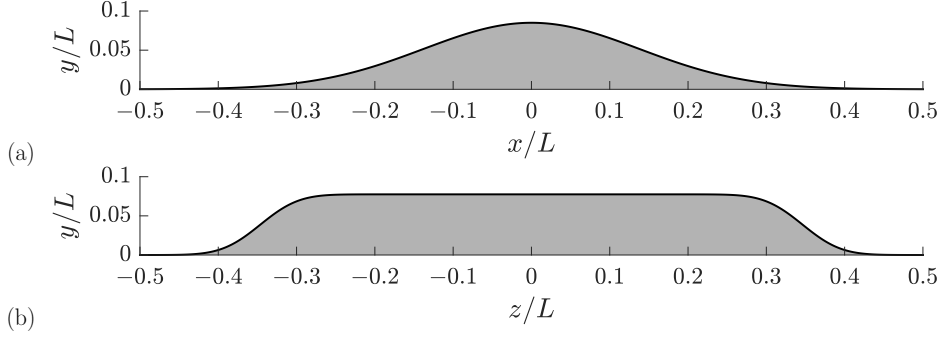


FIG. 11. Cross-sections of the three dimensional bump geometry. The geometry has side walls at  $z/L = \pm 0.5$  and a top wall at  $y/L = 0.5$ . Note that the spanwise-periodic bump has the same cross-sectional profile as the three-dimensional bump, however, the spanwise direction is periodic with  $z/L$  spanning from 0 – 0.08, and the top wall is at  $y/L = 1.0$ .

Mesh	$N_{cv}$	$\max \Delta/L$	$\min \Delta/L$
Coarse	3 Mil.	0.01	$1.3 \times 10^{-3}$
Medium	12 Mil.	0.01	$6.3 \times 10^{-4}$
Fine	52 Mil.	0.01	$3.1 \times 10^{-4}$

TABLE II. Mesh parameters for the spanwise-periodic bump case at  $Re_L = 2 \times 10^6$ .

cells thick) of twice refined cells in all directions into the regions immediately adjacent to the bump. Lloyd iterations are employed to smooth the mesh at transitions in resolution; the result is a nearly centroidal mesh. The same refinement strategy for the spanwise-periodic and three-dimensional configurations facilitates comparison between them. Three computational mesh sizes are studied in the present work, details for which are provided in Tables II and III.

### A. Spanwise-periodic bump at $Re_L = 2 \times 10^6$

In this section we compare WMLES results with quasi-DNS data for the spanwise-periodic geometry at upstream Reynolds number,  $Re_L = \rho_\infty U_\infty L / \mu_\infty = 2 \times 10^6$  where  $\mu_\infty$  and  $\rho_\infty$  are the free-stream dynamic viscosity and density respectively.

In Figure 12, skin friction coefficients are compared across the three meshes for DSM, DTCSM and the Vreman model. The friction coefficient at the inlet is different from that of the quasi-DNS likely due to the difference in inlet boundary conditions (more details in Whitmore et al. [54]). Similar to previous observations [54], the coarse mesh results predict flow separation (albeit slightly under-predicted) using DSM. On refinement, the separation is diminished and then reappears on further refinement up to the fine mesh. At the fine mesh resolution, the separation bubble size is in good agreement with DNS for both DSM and DTCSM. It is noteworthy that DTCSM shows a monotonic convergence toward the DNS  $C_f$ , particularly in the region of separation. This is in contrast to the results from the DSM and Vreman models, which both predict the separation at coarse resolution, but show the medium resolution results moving away from the DNS solution. The non-monotonic convergence of WMLES towards DNS/experimental results has also been observed in the past with DSM and Vreman model in complex flows [19, 21] where both the models over-predicted the total lift in the linear region of the lift curve upon initial mesh refinement, and the predictions improved upon further refinement.

Since this flow is driven by a favorable pressure gradient in the upstream region of the apex of the bump, there is a substantial increase in the skin friction. DSM under-predicts the peak of skin friction in this flow at the fine mesh

Mesh	$N_{cv}$	$\max \Delta/L$	$\min \Delta/L$
Coarse	29 Mil.	0.01	$1.3 \times 10^{-3}$
Medium	117 Mil.	0.01	$6.3 \times 10^{-4}$
Fine	452 Mil.	0.01	$3.1 \times 10^{-4}$

TABLE III. Mesh parameters for the three dimensional bump case at  $Re_L = 3.41 \times 10^6$ .

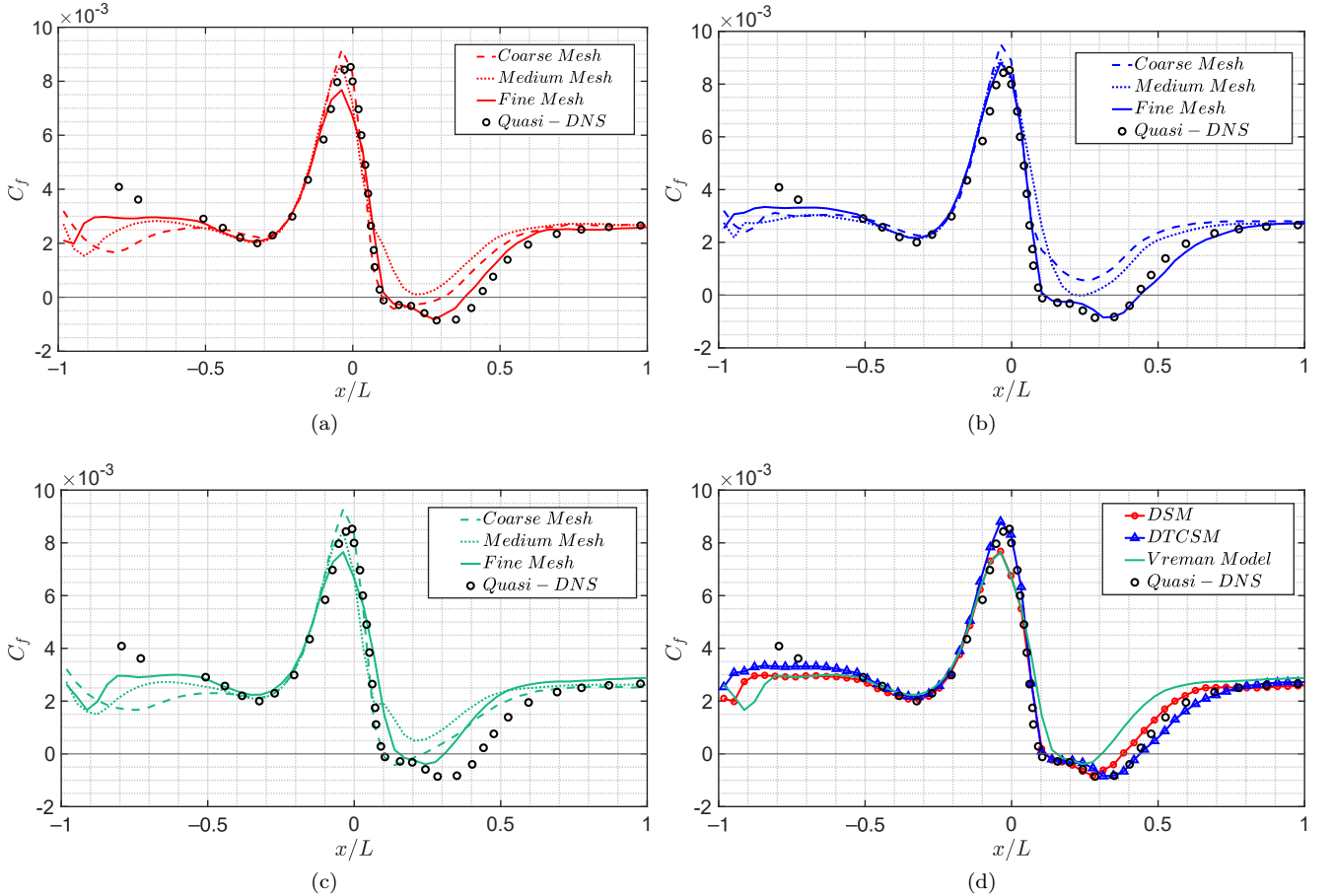


FIG. 12. Streamwise distribution of the surface friction coefficient for the spanwise-periodic bump at  $Re_L = 2 \times 10^6$  for (a) DSM, (b) DTCSTM and (c) Vreman Model. The equilibrium wall model is applied and three mesh resolutions are shown. Finally, sub-figure (d) provides a comparison of the three SGS models for the fine mesh. The black symbols represent the quasi-DNS of Uzun and Malik [50].

resolution (when separation is correctly observed). However, DTCSTM recovers the peak of the skin friction accurately while also predicting the extent of separation. The peak of friction occurs in the region of maximum flow acceleration and anisotropic shear rates, which is consistent with the motivation for the tensorial expansion utilized by DTCSTM (incorporating the effect of anisotropy of large scale structures on the subgrid-scale stresses).

Figure 13 compares the pressure coefficients across the models and mesh sizes. The size of the separation bubble predicted by the Vreman model is smaller and compares less favorably than both dynamic models, even for the most refined grid. This is apparent from the very small flattened region of  $C_p$  downstream of the bump apex in Figure 13 for the Vreman model and also the region of negative  $C_f$  in Figure 12.

### B. Three-dimensional bump at $Re_L = 3.41 \times 10^6$

WMLES results are presented for the full experimental geometry given in Eq. (16) at a higher Reynolds number of  $Re_L = 3.41 \times 10^6$ . Williams et al. [55] and Gray et al. [23] have performed experimental measurements of the surface pressure and skin friction respectively for the three-dimensional bump. Due to the tapering effect of the bump in the spanwise direction which relieves the pressure in the span, two counter-rotating vortices are formed in the separation region [55]. Iyer and Malik [24] observed no separation in their WMLES calculations with the Vreman model with up to 450 Mil. CVs. Previous RANS efforts [24, 55] using the SA-Linear model and the SA-QCR correction model have also been unsuccessful in capturing the correct extent of the separation bubble (Iyer et al. [24] observed weak separation using SA-QCR model). The peak in the pressure in the spanwise direction at the apex of the bump was also absent in these studies.

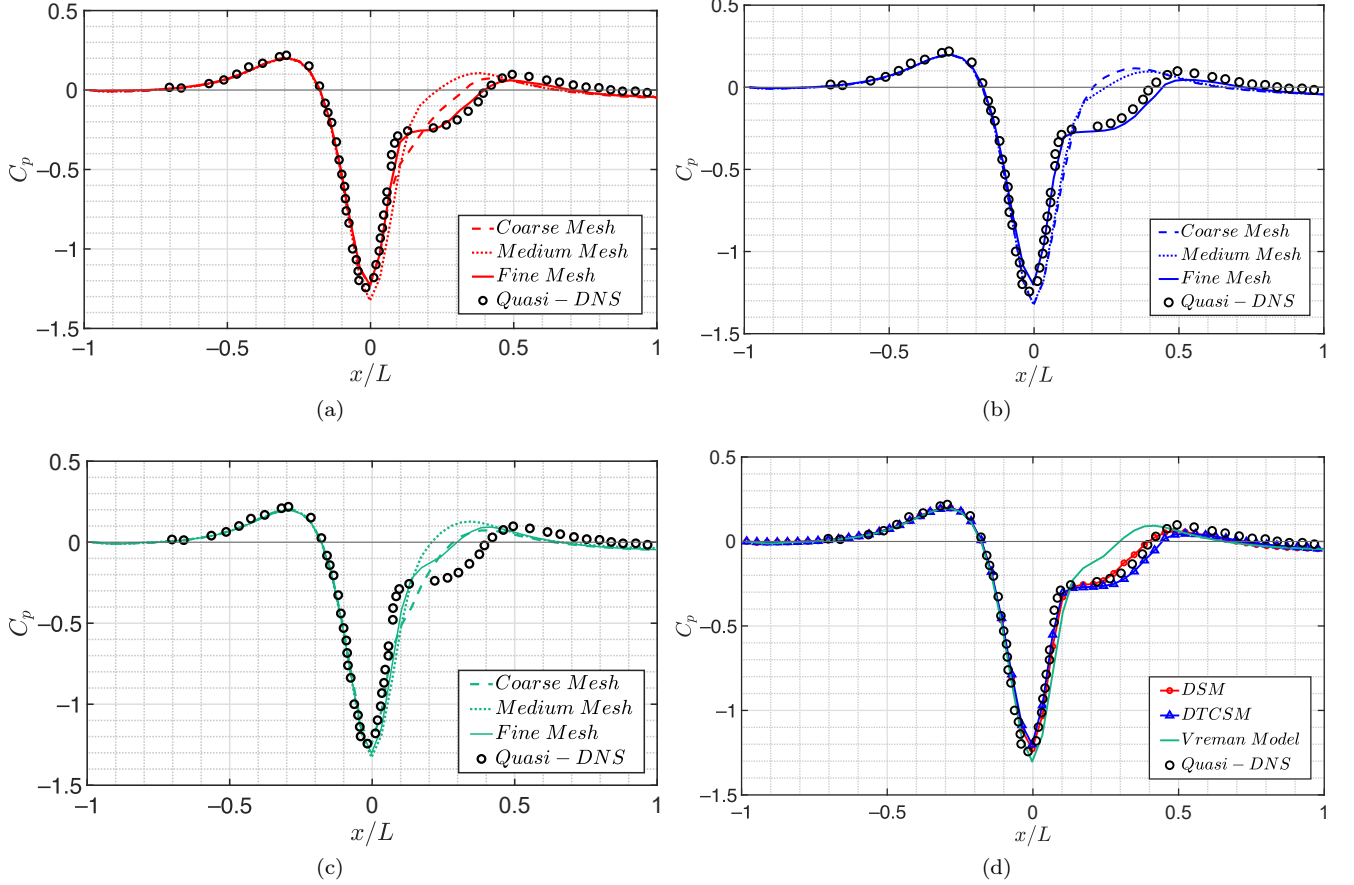


FIG. 13. Streamwise distribution of the surface pressure coefficient for the spanwise-periodic bump at  $Re_L = 2 \times 10^6$  for (a) DSM, (b) DTCSM and (c) constant coefficient Vreman Model. The equilibrium wall model is applied and three mesh resolutions are shown. Finally, sub-figure (d) provides a comparison of the three SGS models for the fine mesh. The black symbols represent the quasi-DNS of Uzun and Malik [50].

As is the case with the spanwise-periodic bump, the skin friction coefficient profile suggests that DSM predicts flow separation (albeit smaller than experiment) on the coarsest grid unlike DTCSM (see Figure 14). On refinement, the separation bubble fails to appear for both DSM and DTCSM. After further refinement, the resolution of the nearest-to-wall cell center in the upstream region of the bump drops to about  $y^+ \sim 30$ . For this fine mesh, the separation bubble reappears for DSM and appears for the first time for DTCSM. The size of the separation bubble is in agreement with the measurements of Gray et al. [23].

The proposed tensor-coefficient model retains its monotonic convergence in the 3D configuration (and higher Reynolds number) unlike DSM. For DTCSM, as the grid is refined, the trough of  $C_f$  moves towards DNS monotonically. The region of maximum flow acceleration ( $x/L \sim -0.1$ ) where the skin friction reaches its peak is also more robust to refinement and more accurate for DTCSM. Figure 15 compares the pressure coefficient at mid-span of the bump, where pressure profile flattens in the separation region. It becomes evident that the fine grid tensor-coefficient model produces excellent agreements with the experiments. The monotonicity of DTCSM also holds for the pressure unlike DSM in that for DTCSM the flow remains attached at coarse and medium grid levels. The suction peak is captured well by both DSM and DTCSM since it is primarily due to inviscid effects. Indeed, the suction peak is accurately predicted in a separate simulation (not shown) with free slip (inviscid) boundary conditions.

An important feature of this three dimensional flow, which is not-observed in the spanwise-periodic case is the variation in pressure across the span of the domain. Figure 16 compares the pressure coefficient variation at the apex of the bump for the fine grid cases. The slight rise in the pressure at mid-span is possibly due to the effect of the counter-rotating vortices that reduces the local streamwise velocity, which increases the local pressure in the region. Both models predict the pressure far away from the mid-span. Near the center, however, it is evident that DTCSM better captures the small and subtle rise in  $C_p$ , likely due to the improved effective body shape from an accurate prediction of the extent of the separation downstream. (Although not shown, our experiments have suggested that

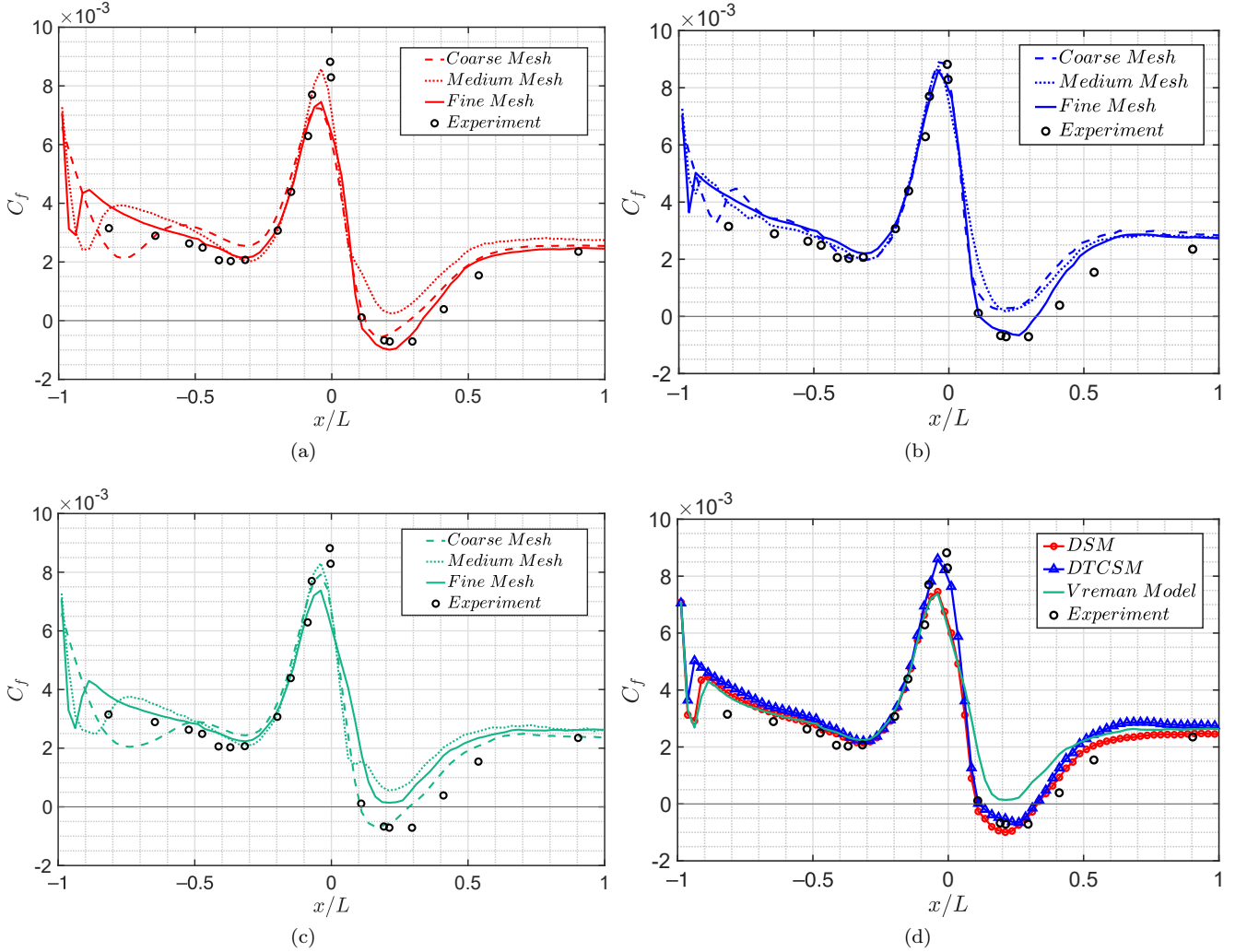


FIG. 14. Streamwise distribution of the mid-span surface friction coefficient for the three dimensional bump at  $Re_L = 3.41 \times 10^6$  for (a) DSM, (b) DTCSM and (c) constant-coefficient Vreman model. The equilibrium wall model is applied and three mesh resolutions are shown. Finally, sub-plot (d) compares the prediction of  $C_f$  by the three models on the fine mesh. The black dots represent the experiments performed by Gray et al. [23].

a larger separation bubble leads to a larger effective stream-wise extent of the bump, which shifts the value of  $C_p$  at the suction peak towards zero).

The relative under-performance of the constant coefficient Vreman model was established in the spanwise-periodic bump. In this three-dimensional flow, however, the differences become even more apparent in that the Vreman model does not predict separation even with the finest grids (refer to Figures 14,15). The issue with the Vreman model is also visible in the pressure prediction across the span at the bump apex where the pressure peak at mid-span is completely missed by the Vreman model (Figure 16).

Previously, comparisons between surface streamlines of skin friction from the LES have been compared with experimental visualizations to qualitatively study the nature of the flow structures [20, 22, 34]. For this flow, Williams et al. [55] performed clay-kerosene mixture based visualizations and observed a pair of counter-rotating vortices in the aft section of the bump. In the current work, we compare the surface skin-friction streamlines with these experimental visualizations. Our simulations with DSM and DTCSM accurately capture the location and size of the strongly vortical region as observed in figure 17. It is also evident that the Vreman model does not capture this vortex-pair, and thus predicts faster (and hence more attached) flow near the wall. The streamlines also reveal the characteristics of the mean circulation in the separated region. For DSM and DTCSM, it is clearly observed that the mean spanwise velocity is directed towards the center near the side walls, and a outward (from center) moving region is present near the mid-span. The Vreman model, on the contrary, does not predict this behavior owing to

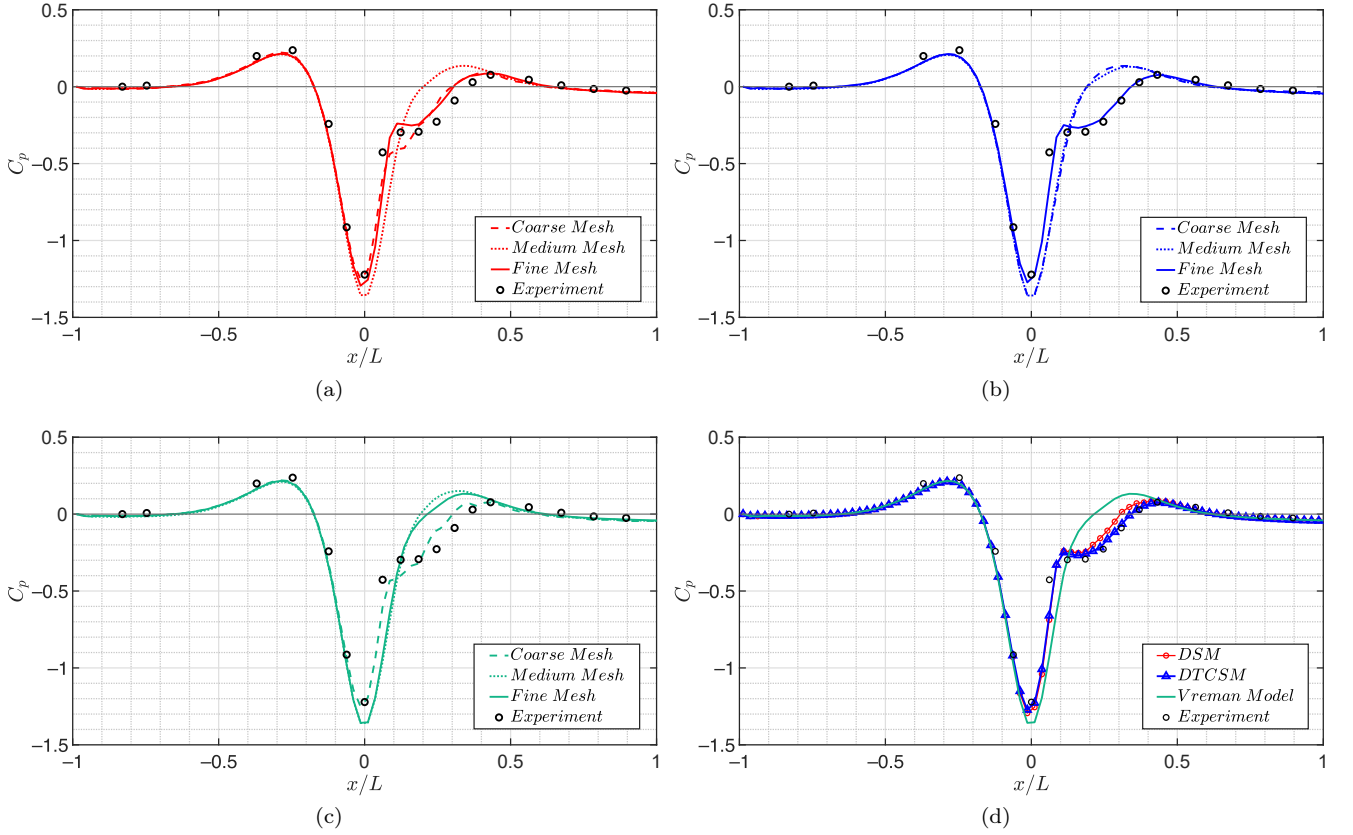


FIG. 15. Streamwise distribution of the mid-span surface pressure coefficient for the three dimensional bump at  $Re_L = 3.41 \times 10^6$  for (a) DSM, (b) DTCSM and (c) constant coefficient Vreman model. Finally, sub-plot (d) provides a comparison of the three models for the fine mesh. The black dots represent the experimental measurements of Williams et al. [55].

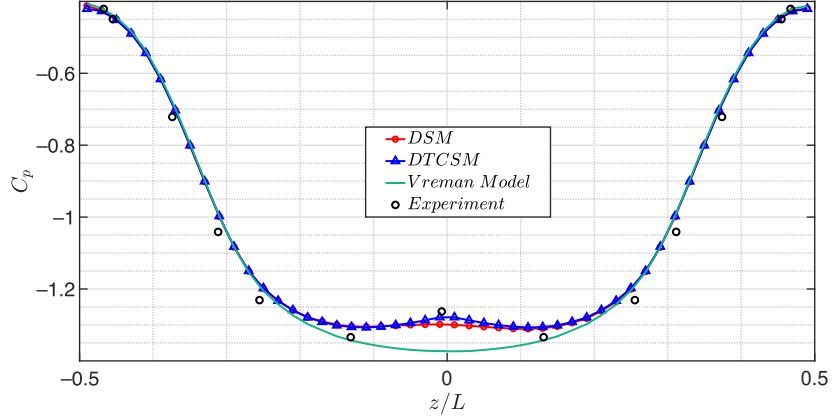


FIG. 16. Spanwise distribution of the surface pressure coefficient for the three dimensional bump at  $Re_L = 3.41 \times 10^6$  for DSM, DTCSM and constant coefficient Vreman model for the fine mesh case. The black dots represent the experiments of Williams et al. [55].

the absence of the separation bubble. This observation is consistent with the surface skin-friction streamlines of Iyer and Malik [24] with the Vreman model. The instantaneous values of the streamwise velocity, projected on the wall from the nearest neighbouring cell for the fine mesh simulation are presented in Figure 18. Both DSM and DTCSM qualitatively behave similarly, in that the flow strongly decelerates (and eventually separates) on passing through the apex (marked by the red region in the subfigures). Since the flow remains attached (in the mean) for the Vreman

model, this deceleration is expected to be much weaker, and is confirmed in our calculations (Figure 18(c)). A vortex-wake extending up to approximately  $x/L \sim 0.5$  is also observed for DSM and DTCSM, which is in agreement to the experimental observations. In this view, the recirculation zone appears to be the strongest for DTCSM, which is in agreement with its higher (and more accurate)  $C_p$  prediction around mid-span.

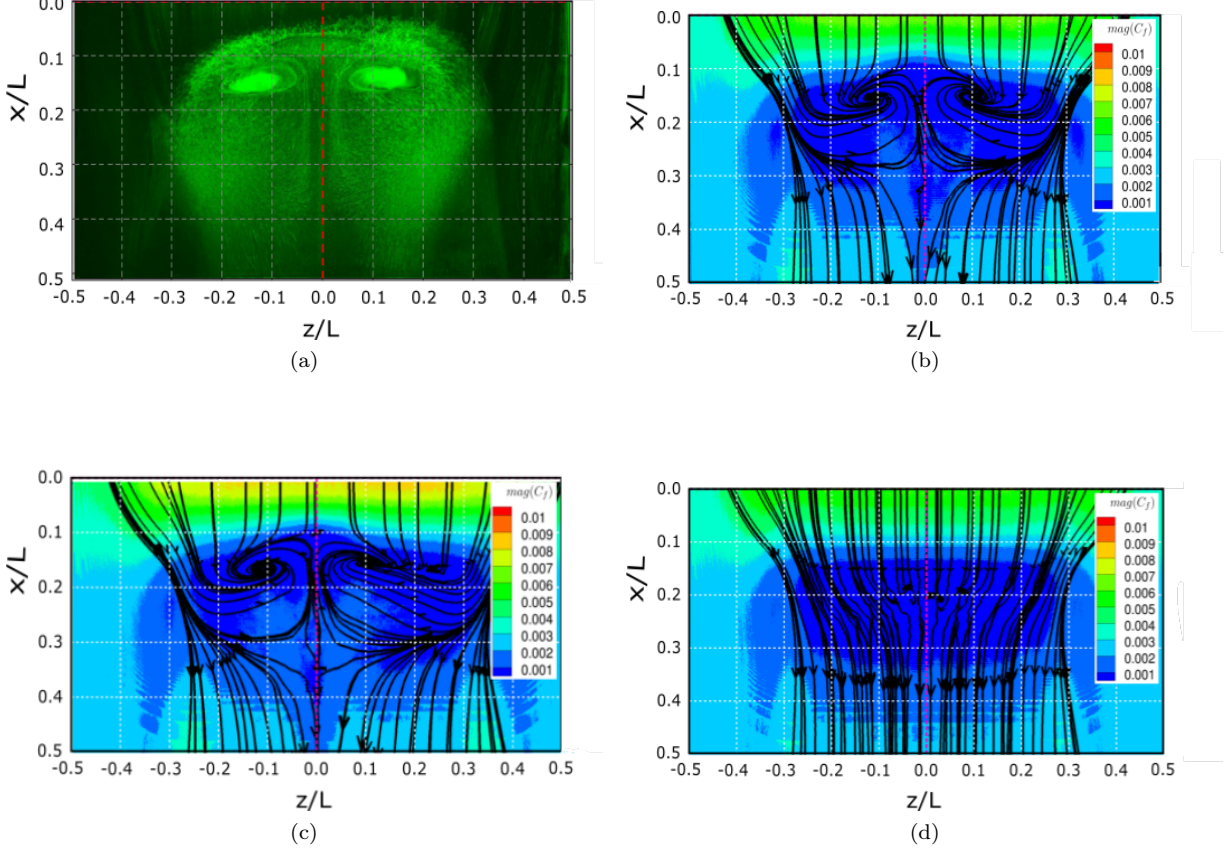


FIG. 17. (a) An oil-flow visualization of the counter-rotating vortices in the region of separation (as observed experimentally [55]); reprinted with permission of the American Institute of Aeronautics and Astronautics, Inc. In sub-plots (b), (c) and (d) we compare the surface streamlines in the separation region for DSM, DTCSM and constant coefficient Vreman models respectively. It is also noticeable that for DTCSM, the skin friction at the apex of the bump is inline with the experimental value and higher than DSM and Vreman models.

## IX. CONCLUSIONS

In this work, we have developed and validated a new non-Boussinesq-type dynamic SGS closure formulation for the tensor-coefficient Smagorinsky model (DTCSM). Similar to the dynamic Smagorinsky model, the only input parameter to this model is the ratio of test-level and grid-level filter widths.

*A priori* calculations have confirmed improved tensor-level correlations of exact SGS stresses and DTCSM. Asymptotic behavior of the model in the near-wall region is in-line with DNS data without the need for damping functions. The model also produces vanishing subgrid-scale stresses in laminar flow. Large-eddy simulations of canonical flows such as decaying and forced HIT at  $Re_\lambda = 70,315$  and  $Re_\lambda \rightarrow \infty$  have been performed. DTCSM performs well in HIT at all Reynolds numbers considered. For wall-modeled LES of a turbulent channel flow at  $Re_\tau = 4200$ , improvements in mean-velocity profile, prediction of the Kármán constant and in mean streamwise, wall-normal intensities near the wall are observed. Finally, it is observed that DTCSM improves the prediction of the skin-friction peak for wall-modeled simulations of the flow over both the spanwise-periodic and three dimensional Gaussian bump at  $Re_L = 2 \times 10^6$  and  $3.41 \times 10^6$  respectively and also does not suffer from non-monotonic convergence towards quasi-DNS unlike DSM. This observation is also of practical interest since traditional LES methodologies rely on a grid refinement procedure to establish confidence in results. For the three-dimensional case, pressure in both the streamwise and spanwise directions are better predicted by DTCSM over DSM. The formation of the counter rotating

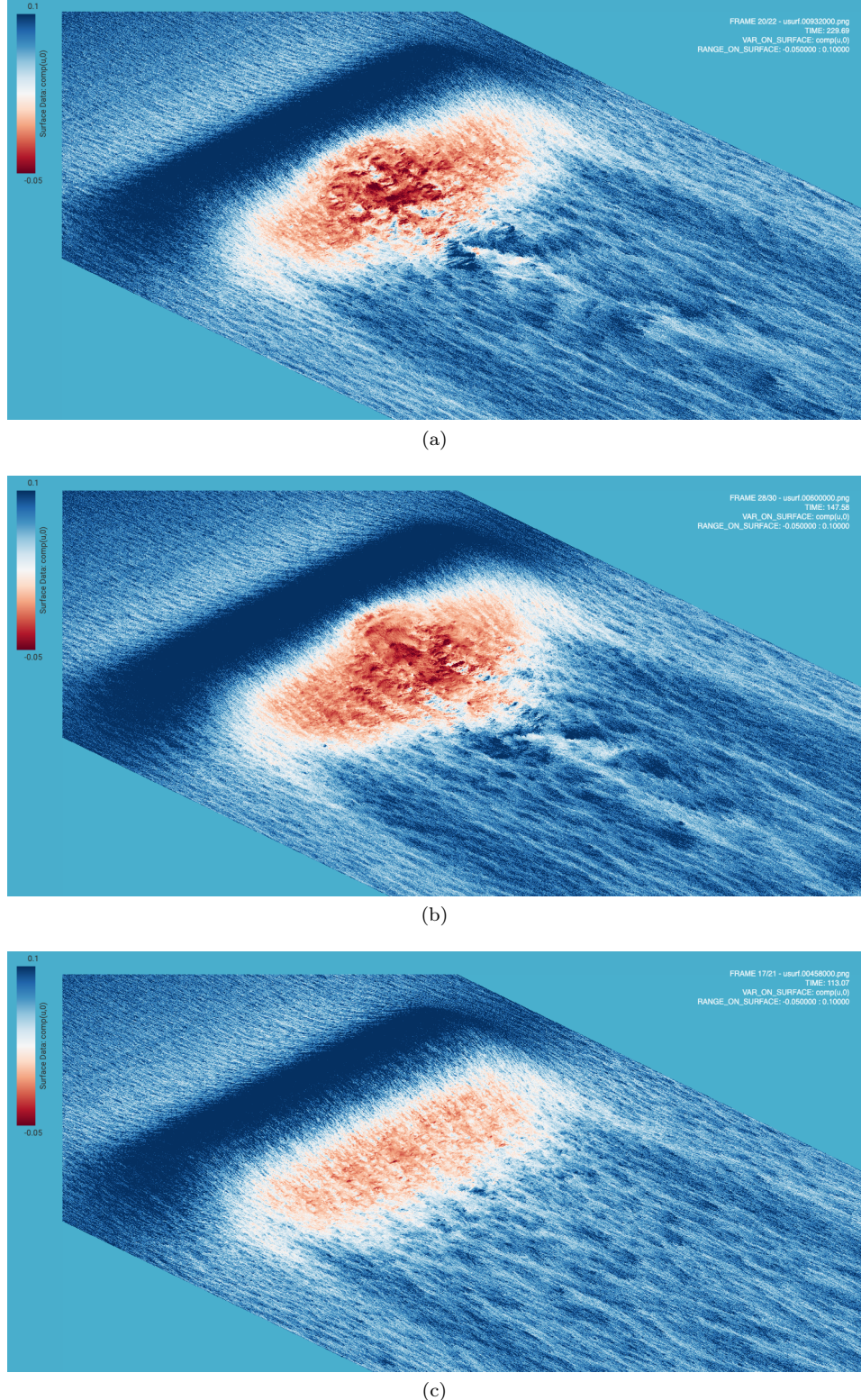


FIG. 18. Oblique view of the instantaneous streamwise velocity for the first grid cell, projected on the bump surface for the fine mesh case. Sub-figures (a), (b), (c) are for DSM, DTCSM and constant-coefficient Vreman models, respectively.

vortex pair in the three dimensional bump is observed for the two dynamic subgrid-scale models in accordance with the experiment. This work is aimed at demonstrating, for the first time, the improvements in predictions from LES

on using a dynamic non-Boussinesq SGS model for both canonical and complex flows involving mean anisotropy and pressure-gradient effects.

## X. ACKNOWLEDGMENTS

R.A. gratefully acknowledges support from the Stanford School of Engineering Fellowship. R.A., M.P.W., S.T.B. and P.M. acknowledge funding from NASA grant no. NNX15AU93A. K.P.G. acknowledges support from the Stanford Graduate Fellowship and the National Defense Science and Engineering Graduate Fellowship. R.A. thanks Ahmed Elnahhas for providing the DNS dataset of a turbulent channel flow at  $Re_\tau = 395$ . We also acknowledge helpful discussions with Konrad Goc. Computing resources were awarded through the Oak Ridge Leadership Computing Facility (DoE ALCC).

---

[1] R. Agrawal, M. Whitmore, K. Griffin, and P. Moin. Dynamic modeling of non-Boussinesq subgrid-scale models for large-eddy simulations. *Center for Turbulence Research Annual Research Briefs*, pages 31–43, 2021.

[2] H. J. Bae and A. Lozano-Durán. Effect of Wall Boundary Conditions on a Wall-Modeled Large-Eddy Simulation in a Finite-Difference Framework. *Fluids*, 6(3):112, 2021.

[3] H. J. Bae, A. Lozano-Durán, S. Bose, and P. Moin. Turbulence intensities in large-eddy simulation of wall-bounded flows. *Physical Review Fluids*, 3(1):014610, 2018.

[4] P. Balakumar and G. I. Park. DNS/LES simulations of separated flows at high Reynolds numbers. In *45th AIAA Fluid Dynamics Conference*, page 2783, 2015.

[5] J. Bardina, J. Ferziger, and W. Reynolds. Improved subgrid-scale models for large-eddy simulation. In *13th fluid and plasmadynamics conference, AIAA Paper*, 1980.

[6] M. Bassenne, J. Urzay, G. I. Park, and P. Moin. Constant-energetics physical-space forcing methods for improved convergence to homogeneous-isotropic turbulence with application to particle-laden flows. *Phys. Fluids*, 28(3):035114, 2016.

[7] S. T. Bose and G. I. Park. Wall-modeled large-eddy simulation for complex turbulent flows. *Annu. Rev. Fluid Mech.*, 50:535–561, 2018.

[8] G. A. Bres, S. T. Bose, M. Emory, F. E. Ham, O. T. Schmidt, G. Rigas, and T. Colonius. Large-eddy simulations of co-annular turbulent jet using a Voronoi-based mesh generation framework. In *2018 AIAA/CEAS Aeroacoustics Conference*, page 3302, 2018.

[9] W. Cabot and P. Moin. Approximate wall boundary conditions in the large-eddy simulation of high Reynolds number flow. *Flow, Turbul. Combust.*, 63(1):269–291, 2000.

[10] J. I. Cardesa, A. Vela-Martín, and J. Jiménez. The turbulent cascade in five dimensions. *Science*, 357(6353):782–784, 2017.

[11] M. Cho, A. Lozano-Durán, P. Moin, and G. Ilhwan Park. Wall-modeled large-eddy simulation of turbulent boundary layers with mean-flow three-dimensionality. *AIAA Journal*, pages 1–11, 2021.

[12] R. A. Clark, J. H. Ferziger, and W. C. Reynolds. Evaluation of subgrid-scale models using an accurately simulated turbulent flow. *J. Fluid Mech.*, 91(1):1–16, 1979.

[13] G. Comte-Bellot and S. Corrsin. Simple Eulerian time correlation of full-and narrow-band velocity signals in grid-generated, ‘isotropic’ turbulence. *J. Fluid Mech.*, 48(2):273–337, 1971.

[14] J. W. Deardorff. A numerical study of three-dimensional turbulent channel flow at large Reynolds numbers. *J. Fluid Mech.*, 41(2):453–480, 1970.

[15] D. M. Driver and H. L. Seegmiller. Features of a reattaching turbulent shear layer in divergent channel flow. *AIAA journal*, 23(2):163–171, 1985.

[16] L. Fu, M. Karp, S. T. Bose, P. Moin, and J. Urzay. Shock-induced heating and transition to turbulence in a hypersonic boundary layer. *J. Fluid Mech.*, 909, 2021.

[17] M. Germano, U. Piomelli, P. Moin, and W. H. Cabot. A dynamic subgrid-scale eddy viscosity model. *Phys. Fluids A: Fluid Dynamics*, 3(7):1760–1765, 1991.

[18] S. Ghosal, T. S. Lund, P. Moin, and K. Akselvoll. A dynamic localization model for large-eddy simulation of turbulent flows. *J. Fluid Mech.*, 286:229–255, 1995.

[19] K. Goc, S. Bose, and P. Moin. Subgrid-scale modeling sensitivities in wall-modeled large-eddy simulations of a high-lift aircraft configuration. *Annual Research Briefs*, pages 49–58, 2020.

[20] K. Goc, S. Bose, and P. Moin. Wall-modeled large eddy simulation of an aircraft in landing configuration. In *AIAA Aviation 2020 Forum*, page 3002, 2020.

[21] K. Goc, S. Bose, and P. Moin. Large-eddy simulation of the NASA high-lift common research model. *Center for Turbulence Research Annual Research Briefs*, pages 3–16, 2021.

[22] K. A. Goc, O. Lehmkuhl, G. I. Park, S. T. Bose, and P. Moin. Large eddy simulation of aircraft at affordable cost: a milestone in computational fluid dynamics. *Flow*, 1, 2021.

[23] P. D. Gray, I. Gluzman, F. O. Thomas, and T. C. Corke. Experimental Characterization of Smooth Body Flow Separation Over Wall-Mounted Gaussian bump. In *AIAA SCITECH 2022 Forum*, page 1209, 2022.

[24] P. S. Iyer and M. R. Malik. Wall-modeled LES of flow over a Gaussian bump. In *AIAA Scitech 2021 Forum*, page 1438, 2021.

[25] S. Kawai and J. Larsson. Wall-modeling in large eddy simulation: Length scales, grid resolution, and accuracy. *Physics of Fluids*, 24(1):015105, 2012.

[26] S. Kawai and J. Larsson. Dynamic non-equilibrium wall-modeling for large eddy simulation at high Reynolds numbers. *Phys. Fluids*, 25(1):015105, 2013.

[27] J. Kim, P. Moin, and R. Moser. Turbulence statistics in fully developed channel flow at low Reynolds number. *Journal of Fluid Mechanics*, 177:133–166, 1987.

[28] M. T. Lakebrink, M. Mani, E. Rolfe, J. T. Spyropoulos, D. Philips, S. Bose, and J. Mace. Toward improved turbulence-modeling techniques for internal-flow applications. In *AIAA Aviation 2019 Forum*, page 3703, 2019.

[29] A. Leonard. Energy cascade in large-eddy simulations of turbulent fluid flows. In *Adv. Geophys.*, volume 18, pages 237–248. Elsevier, 1975.

[30] D. Lilly. Progress in Research in Atmospheric Turbulence, NCAR manuscript 70-182. *National Center for Atmospheric Research Boulder, Colorado*, 1970.

[31] D. K. Lilly. On the application of the eddy viscosity concept in the inertial sub-range of turbulence. *NCAR manuscript*, 123, 1966.

[32] D. K. Lilly. A proposed modification of the Germano subgrid-scale closure method. *Phys. Fluids A: Fluid Dynamics*, 4(3):633–635, 1992.

[33] A. Lozano-Durán and H. J. Bae. Error scaling of large-eddy simulation in the outer region of wall-bounded turbulence. *J. Comput. Phys.*, 392:532–555, 2019.

[34] A. Lozano-Durán, S. T. Bose, and P. Moin. Performance of wall-modeled les for external aerodynamics in the nasa juncture flow. *arXiv preprint arXiv:2101.00331*, 2021.

[35] A. Lozano-Durán and J. Jiménez. Effect of the computational domain on direct simulations of turbulent channels up to  $Re_\tau = 4200$ . *Phys. Fluids*, 26(1):011702, 2014.

[36] T. S. Lund and E. Novikov. Parameterization of subgrid-scale stress by the velocity gradient tensor. *Annual Research Briefs*, 1992:27–43, 1992.

[37] N. Mansour, P. Moin, W. Reynolds, and J. Ferziger. Improved methods for large eddy simulations of turbulence. In *Turbulent shear flows I*, pages 386–401. Springer, 1979.

[38] P. Moin. A new approach for large eddy simulation of turbulence and scalar transport. In *Dracos, T. & Tsinober, A. (Eds.), New Approaches and Concepts in Turbulence*, pages 331–339. Springer, 1993.

[39] P. Moin and J. Kim. Numerical investigation of turbulent channel flow. *J. Fluid Mech.*, 118:341–377, 1982.

[40] Y. Morimishi and O. V. Vasilyev. Vector level identity for dynamic subgrid scale modeling in large eddy simulation. *Phys. Fluids*, 14(10):3616–3623, 2002.

[41] F. Nicoud and F. Ducros. Subgrid-scale stress modelling based on the square of the velocity gradient tensor. *Flow, turbulence and Combustion*, 62(3):183–200, 1999.

[42] F. Nicoud, H. B. Toda, O. Cabrit, S. Bose, and J. Lee. Using singular values to build a subgrid-scale model for large eddy simulations. *Physics of fluids*, 23(8):085106, 2011.

[43] T. Passot and A. Pouquet. Numerical simulation of compressible homogeneous flows in the turbulent regime. *J. Fluid Mech.*, 181:441–466, 1987.

[44] U. Piomelli. High Reynolds number calculations using the dynamic subgrid-scale stress model. *Phys. Fluids A: Fluid Dynamics*, 5(6):1484–1490, 1993.

[45] U. Piomelli, P. Moin, and J. H. Ferziger. Model consistency in large eddy simulation of turbulent channel flows. *The Physics of fluids*, 31(7):1884–1891, 1988.

[46] H. Pouransari, M. Mortazavi, and A. Mani. Parallel variable-density particle-laden turbulence simulation. *arXiv preprint arXiv:1601.05448*, 2016.

[47] W. Rozema, H. J. Bae, P. Moin, and R. Verstappen. Minimum-dissipation models for large-eddy simulation. *Phys. Fluids*, 27(8):085107, 2015.

[48] A. Seifert and L. G. Pack. Active flow separation control on wall-mounted hump at high Reynolds numbers. *AIAA journal*, 40(7):1363–1372, 2002.

[49] J. Smagorinsky. General circulation experiments with the primitive equations: I. The basic experiment. *Mon. Weather Rev.*, 91(3):99–164, 1963.

[50] A. Uzun and M. R. Malik. High-fidelity simulation of turbulent flow past Gaussian bump. *AIAA Journal*, (to appear).

[51] E. R. Van Driest. On turbulent flow near a wall. *J. Aeronaut. Sci.*, 23(11):1007–1011, 1956.

[52] O. V. Vasilyev, T. S. Lund, and P. Moin. A general class of commutative filters for LES in complex geometries. *Journal of Computational Physics*, 146(1):82–104, 1998.

[53] A. Vreman. An eddy-viscosity subgrid-scale model for turbulent shear flow: Algebraic theory and applications. *Phys. Fluids*, 16(10):3670–3681, 2004.

[54] M. Whitmore, K. Griffin, S. Bose, and P. Moin. Large-eddy simulation of a Gaussian bump with slip-wall boundary conditions. *Center for Turbulence Research Annual Research Briefs*, pages 45–58, 2021.

[55] O. Williams, M. Samuell, E. S. Sarwas, M. Robbins, and A. Ferrante. Experimental study of a CFD validation test case for turbulent separated flows. In *AIAA Scitech 2020 Forum*, page 0092, 2020.

### Appendix A: Proof of tracelessness of DTCSM

In this appendix, we show that DTCSM is traceless with the constraints imposed in Eq. (12). This property is required for consistency as the quantity that is being modeled, the deviatoric part of the subgrid-scale stress tensor, is trace-free by definition. Recall that the model formulation of DTCSM is

$$\tau_{ij}^{sgs} - \frac{\tau_{kk}^{sgs}}{3} \delta_{ij} = -(C_{ik}S_{kj} + C_{jk}S_{ki})|S|\Delta^2. \quad (\text{A1})$$

The trace of the right-hand side of Eq. A1 is

$$\text{trace} [-(C_{ik}S_{ki} + C_{ik}S_{ki})|S|\Delta^2] = -2C_{ik}S_{ki}|S|\Delta^2, \quad (\text{A2})$$

which is further expanded as

$$-2C_{ik}S_{ki}|S|\Delta^2 = -2|S|\Delta^2 \{C_{11}S_{11} + C_{22}S_{22} + C_{33}S_{33} + S_{12}(C_{12} + C_{21}) + S_{13}(C_{13} + C_{31}) + S_{23}(C_{23} + C_{32})\}. \quad (\text{A3})$$

Assuming that the flow is incompressible ( $S_{ii} = 0$ ) and that  $S_{ij}$  is a general strain-rate tensor, we impose

$$C_{11} = C_{22} = C_{33}; \quad C_{ij} = -C_{ji} \quad (j \neq i), \quad (\text{A4})$$

which ensures that the subgrid stress predicted by DTCSM is trace-free.

### Appendix B: System of equations for dynamic procedure in DTCSM

Recall for DTCSM, the Germano identity is written as

$$L_{ij} = (C_{ik}\Delta^2 M_{kj} + C_{jk}\Delta^2 M_{ki}). \quad (\text{B1})$$

Absorbing the factor of  $\Delta^2$  into the coefficients  $C_{ij}$ , and including only the free coefficients of  $C_{ij}$ , the system can be rewritten as

$$\begin{pmatrix} L_{11} \\ L_{22} \\ L_{33} \\ L_{12} \\ L_{13} \\ L_{23} \end{pmatrix} = \begin{pmatrix} 2M_{11} & 2M_{12} & 2M_{13} & 0 \\ 2M_{22} & -2M_{12} & 0 & 2M_{23} \\ 2M_{33} & 0 & -2M_{13} & -2M_{23} \\ 2M_{12} & M_{22} - M_{11} & M_{23} & M_{13} \\ 2M_{13} & M_{23} & M_{33} - M_{11} & -M_{12} \\ 2M_{23} & -M_{13} & -M_{12} & M_{33} - M_{22} \end{pmatrix} \begin{pmatrix} C_{11} \\ C_{12} \\ C_{13} \\ C_{23} \end{pmatrix}, \quad (\text{B2})$$

which, by defining the  $6 \times 4$  matrix on the right-hand side as  $M_{mat}$ , and  $[\cdot]$  as the vectorization operator, can be written concisely as

$$[L] = M_{mat}[C]. \quad (\text{B3})$$

Using the least-squares solutions approach, we get

$$M_{mat}^T [L] = M_{mat}^T M_{mat}[C]. \quad (\text{B4})$$

Finally, Eq. (B4) is solved directly to dynamically evaluate the four model coefficients.

### Appendix C: Another representation of DTCSM

In this appendix, we re-express the model form of DTCSM in terms of a combination of the strain-rate and rotation-rate tensor. In general, the stresses from DTCSM are expressed as

$$\tau_{ij}^{DTCSM} = -(C_{ik}S_{kj} + C_{jk}S_{ki})|S|\Delta^2. \quad (\text{C1})$$

Using the realizability constraints on DTCSM, and decomposing the model coefficient matrix  $C_{ij}$  into isotropic and deviatoric parts,  $C_{ij} = C_{11}\delta_{ij} + C_{ij}^d$ , we write

$$\tau_{ij}^{DTCSM} = - \{ (C_{11}\delta_{ik} + C_{ik}^d)S_{kj} + (C_{11}\delta_{jk} + C_{jk}^d)S_{ki} \} |S|\Delta^2 . \quad (C2)$$

Since the deviatoric part of the coefficient matrix  $C_{ij}^d$  is constrained to be anti-symmetric, it therefore has properties similar to those of the rotation-rate tensor. Setting  $|S|C_{ij}^d = -\Lambda R_{ij}$ , Eq. (C2), the model can be simplified to the form

$$\tau_{ij}^{DTCSM} = -2C_{11}\Delta^2 S_{ij}|S| - \Lambda\Delta^2 (S_{ik}R_{kj} - R_{ik}S_{kj}) , \quad (C3)$$

which is the same model form as the two-term expansion of the velocity gradient tensor in the previous work of Lund and Novikov [36] and a recent study by Agrawal et al. [1]. Hence, under certain scenarios, DTCSM can be interpreted as a model which explicitly accounts for effect of large-scale rotation rates unlike DSM. This is desirable since the production mechanism in 3D turbulence is driven by vortex stretching.